Nano Research

Open Access

Research Article

Intrinsic field-free superconducting diode effect in a simple van der Waals FeSe nanosheet

Yechao Han[1,2,§], Guojing Hu[1,2,§], Zouyouwei Lu[1,2], Senhao Lv[2], Zhen Zhao[2], Jie Liu[1,2], Jinan Shi[1], Hui Guo[2], Lihong Bao[1,2], Xiaoli Dong[2], Wu Zhou[1], Haitao Yang[1,2] ✉, Xiao Lin[1] ✉, and Hong-jun Gao[1,2] ✉

[1] *School of Physical Sciences, University of Chinese Academy of Sciences, Beijing 100049, China*
[2] *Beijing National Center for Condensed Matter Physics and Institute of Physics, Chinese Academy of Sciences, Beijing 100190, China*
[§] *Yechao Han and Guojing Hu contributed equally to this work.*

Cite this article: *Nano Research*, **2026**, *19*, 94908621. https://doi.org/10.26599/NR.2026.94908621

ABSTRACT: Superconducting diodes, characterized by the unidirectional supercurrent flow, are essential components for constructing energy-efficient superconducting circuits. Although the superconducting diode effect has been reported in a wide variety of platforms, its implementation usually requires an external magnetic field, cryogenic temperatures and elaborate device geometries, which significantly limit practical applications. Here, we report an intrinsic, field-free superconducting diode effect in a simple van der Waals FeSe nanosheet. Systematic investigations of sample geometries, residual magnetic fields, Joule heating effects, random vortex trappings, and electrodes or interfacial contacts reveal that the field-free superconducting diode effect originates from the time-reversal-symmetry breaking in the superconducting state of the FeSe nanosheet. The intrinsic field-free superconducting diode effect provides strong evidence of time-reversal-symmetry breaking in FeSe nanosheets. Furthermore, the field-free superconducting diode manifests a stable half-wave rectification performance after the 400-cycle operation and maintains the same polarity over a wide range of both positive and negative magnetic fields, which can tolerate ubiquitous stray fields in electrical circuits. The intrinsic field-free superconducting diode effect in a single van der Waals FeSe nanosheet with a simplified device architecture holds considerable promise for paving the way to practical, scalable superconducting diodes in ultra-low-power electronics.

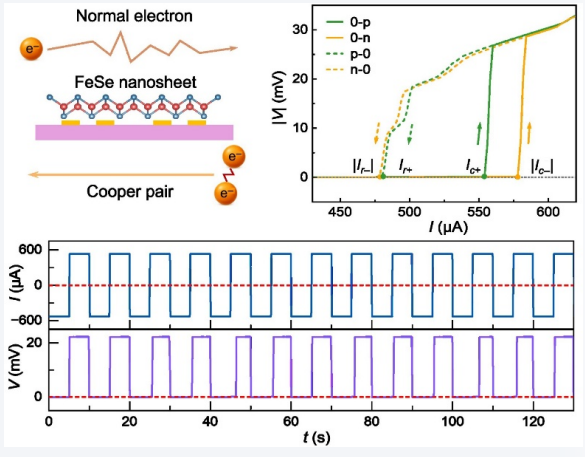

KEYWORDS: field-free superconducting diode effect, van der Waals, FeSe, time-reversal-symmetry breaking

1 Introduction

Diodes [1–3] serve as fundamental building blocks for numerous (opto)electronic technologies, including current rectifiers, voltage-controlled oscillators, AC–DC converters, and photo-detectors. As analog to the semiconductor diode, the superconducting diode effect (SDE) manifests as the non-dissipative, unidirectional flow of supercurrents [4–6]. This phenomenon opens an avenue for analogous applications in superconducting electronics, superconducting spintronics, and quantum information technologies [7–9]. SDE has been experimentally realized in various Josephson junctions [10–20] and junction-free superconductors [21–30]. However, most implementations to date rely on an externally applied magnetic field [10, 12, 19–23, 26, 27] and involve complex device architectures [10–25, 27, 30], which limits their practical application and large-scale integration [31, 32]. Therefore, realizing a field-free SDE in a single superconducting material is crucial for advancing practical implementations.

Thus far, an intrinsic field-free SDE has been reported only in the kagome superconductor CsV_3Sb_5 flakes [28] and the high-temperature cuprate $Bi_2Sr_2CaCu_2O_{8+\delta}$ (BSCCO) flakes [29]. However, the low superconducting transition temperature of CsV_3Sb_5 (T_c: ~ 2.5 K) [33, 34] and the poor environmental stability of BSCCO pose significant challenges for practical applications [35, 36]. Given these limitations, the exploration of alternative superconductors hosting an intrinsic field-free SDE is essential.

Received: January 12, 2026; **Revised:** March 4, 2026
Accepted: March 6, 2026

✉Address correspondence to Haitao Yang, htyang@iphy.ac.cn; Xiao Lin, xlin@ucas.ac.cn; Hong-jun Gao, hjgao@iphy.ac.cn

FeSe, a prototypical van der Waals (vdW) iron-based superconductor with a superconducting transition temperature of 9 K, has shown evidence of time-reversal symmetry (TRS) breaking in previous studies [37–40], suggesting significant potential for achieving the field-free SDE. Nevertheless, the intrinsic field-free SDE in FeSe has not yet been experimentally demonstrated, and its underlying mechanisms remain elusive.

In this work, we fabricated a series of FeSe nanodevices based on high-quality single crystals and observed a reproducible field-free SDE in vdW FeSe nanosheets. By systematically varying device geometries, probing the magnetic-field dependence, and examining thermal perturbations, we demonstrate that the field-free SDE originates from the intrinsic property of FeSe nanosheets rather than from the extrinsic factors, including sample geometries, residual magnetic fields, Joule heating effects, random vortex trappings and electrodes or interfacial contacts. The most plausible microscopic origin is the spontaneous breaking of time-reversal and inversion symmetries in FeSe nanosheets. It is fundamentally distinct from the previously reported field-free SDE in FeSe induced by geometric asymmetry combined with a thermoelectric response [41]. The superconducting diode keeps the same polarity over a wide range of both positive and negative magnetic fields and achieves a stable half-wave rectification after 400 operational cycles. The intrinsic, field-free SDE demonstrated in a simple vdW FeSe nanosheet provides the strong evidence for symmetry breaking in FeSe superconductors and highlights the significant potential for the future energy-efficient computing in two-dimensional information technology.

2 Results and discussion

2.1 Characterizations and superconductivity of the FeSe crystal

FeSe adopts a vdW layered structure (Fig. 1(a)), which is composed of Se-Fe-Se triple layers stacked along the *c* axis, with adjacent monolayers bound together by weak vdW forces. Tetragonal FeSe single crystals with an average size of 1.8 mm (inset of Fig. 1(b)) were synthesized by the chemical vapor transport (CVT) method. As shown in Fig. 1(b), the X-ray diffraction (XRD) pattern of FeSe exhibits (00*l*)-oriented diffraction peaks and the rocking curve obtained from the (001) reflection reveals a minimal full-width-half-maximum (FWHM) value of ~ 0.15°, confirming the high quality of FeSe single crystals. Both the temperature-dependent magnetic susceptibility and electrical resistance measurements of the bulk FeSe crystal (Fig. 1(c)) reveal a sharp superconducting transition at T_c = 8.9 K.

The atomic structure and crystal quality are further characterized using aberration-corrected scanning transmission electron microscope (STEM). Large-area atomic-resolution STEM images acquired on the *ab*-plane (Fig. 1(d)) and *ac*-plane (Fig. 1(e)) show a defect-free lattice that matches the crystallographic model (inset). The nearest-neighbor Fe–Fe spacing measured from the image is 0.277 nm (Fig. S2(a) in the Electronic Supplementary Material (ESM)), consistent with the lattice parameter of 0.278 nm. To probe the possible Fe intercalation between adjacent layers, cross-sectional STEM images are performed on the *ac*-plane at different regions. All STEM images (Fig. 1(e) and Fig. S3 in the ESM) and the cross-sectional energy-dispersive X-ray spectroscopy (EDS) elemental spatial mappings (Fig. 1(f)) display the expected layered stacking without detectable intercalated Fe atoms.

2.2 Field-free SDE of the FeSe nanosheet with an asymmetric geometric shape

Based on the high-quality FeSe crystal, a piece of FeSe nanosheet with a uniform thickness of 10 nm, determined by atomic force microscopy (AFM) (Fig. S4(a) in the ESM) is exfoliated and transferred onto a pre-prepared parallel four-electrode. The nanosheet is then encapsulated with a top hexagonal boron nitride (hBN) layer to avoid the oxidation and degradation, which is

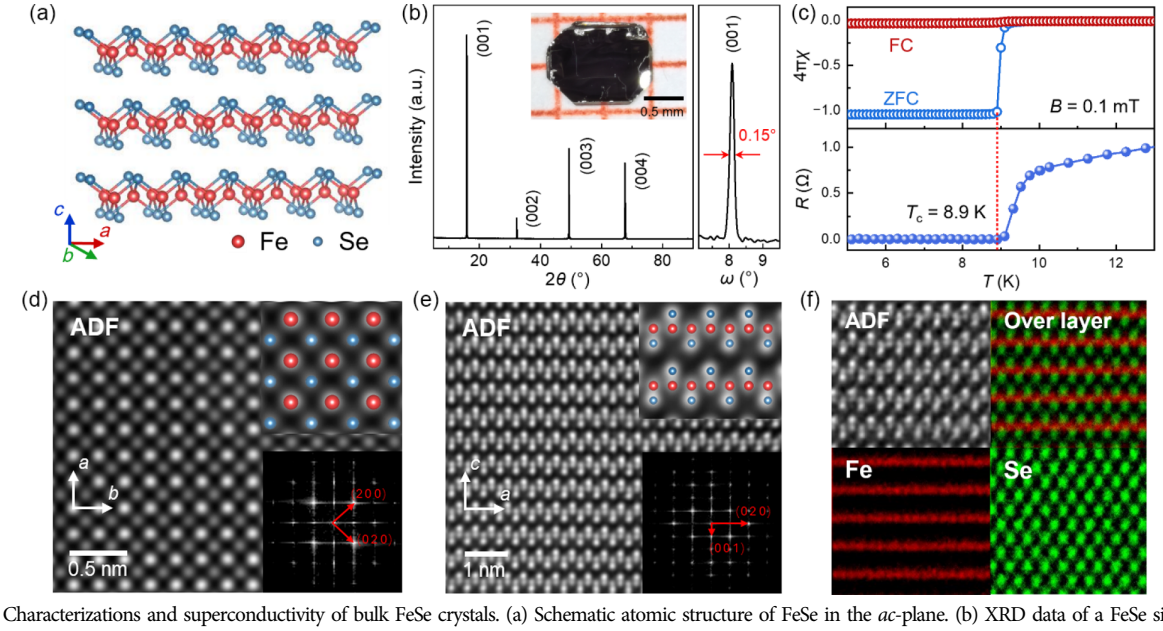

Figure 1 Characterizations and superconductivity of bulk FeSe crystals. (a) Schematic atomic structure of FeSe in the *ac*-plane. (b) XRD data of a FeSe single crystal: (Left) (00l) diffraction peaks of FeSe with the inset showing the image of the as-grown FeSe crystal. (Right) Rocking curve of (001) peak with FWHM = 0.15°. (c) Temperature-dependent magnetic susceptibility and resistance of the FeSe crystal, revealing T_c = 8.9 K. (d) and (e) STEM-ADF images of FeSe crystal in the *ab*-plane and *ac*-plane, respectively. The corresponding atomic models and FFT patterns are shown in the insets. (f) STEM-EDS elemental spatial mapping of Fe (red) and Se (green) relative to *ac*-plane.

defined as Device #1. As shown in Fig. 2(a), the FeSe nanosheet in Device #1 possesses an intentionally asymmetric geometry. When Device #1 is cooled to a low temperature under the zero magnetic field, the temperature-dependent resistance exhibits a broad superconducting transition. The transition begins at the onset temperature T_c^{onset} = 6.1 K and reaches the zero-resistance state at T_c^{zero} = 4.7 K (Fig. 2(b)). The measured voltage–current (*V*–*I*) characteristics of Device #1 at 2 K under the zero magnetic field are shown in Fig. S5(a) in the ESM. The *V*–*I* curve exhibits a distinct hysteresis loop that can be divided into four branches: from zero to positive (0-p), positive to zero (p-0), zero to negative (0-n), and negative to zero (n-0).

Critical current (I_c) is defined at the superconducting-to-normal transition, while the returning current (I_r) corresponds to the normal-to-superconducting transition. Accordingly, the positive-bias branch yields I_{c+} and I_{r+}, the negative-bias branch yields I_{c-} and I_{r-}. To clearly visualize the asymmetry of the critical currents, the negative-bias branch of the *V*–*I* curve is inverted and superimposed onto the positive-bias region (Fig. 2(c)). The absolute value of I_{c-} is larger than that of I_{c+}, with a difference ΔI_c of 24 μA ($\Delta I_c = |I_{c-}| - I_{c+}$), clearly demonstrating a pronounced field-free SDE in the FeSe nanosheet with an asymmetric geometric shape.

To elucidate the nonreciprocal behavior in Device #1, systematic electrical transport measurements are performed. The *V*–*I* curves at varying temperatures are measured (Fig. S5(b) in the ESM), and the critical currents I_{c+} and I_{c-} are extracted from the *V*–*I* curves. As shown in Fig. 2(d), temperature-dependent critical currents I_{c+} and I_{c-} in Device #1 show a monotonical decrease as the temperature increases, while $|I_{c-}|$ is always larger than I_{c+} below the temperature of 3.5 K, indicating an obvious SDE in the low-temperature superconducting regime. To further investigate the field-free nature of SDE, the magnetic field dependence of critical currents in Device #1 is measured. The *V*–*I* curves are recorded when sweeping the out-of-plane magnetic field from −100 to +100 mT at 2 K (Fig. S5(c) in the ESM), and the magnetic field dependence of I_{c+} and $|I_{c-}|$ is extracted and plotted in Fig. 2(e). The data points of $|I_{c-}|$ are always above I_{c+} between B = ±50 mT, showing a robust SDE regardless of reversing the magnetic field direction. This even, field-symmetric dependence of ΔI_c is distinct from the antisymmetric behavior reported for the field-induced SDE, indicating that the observed SDE is not attributed to the magnetochiral anisotropy. Furthermore, we have performed the square-wave rectification measurement on Device #1 by leveraging this field-free SDE. As shown in Fig. 2(f), a 0.1 Hz square-wave excitation current of 0.562 mA exceeding I_{c+} (0.554 mA) but below $|I_{c-}|$ (0.578 mA) triggers the distinct superconducting-to-resistive transition. The negative half-cycles maintain the superconducting state, whereas the positive half-cycles drive the device into the normal state, producing finite voltages larger than 20 mV, which yields an on/off voltage ratio exceeding 10^4.

2.3 Field-free SDE of the FeSe nanosheet with a symmetric geometric shape

In contrast to Device #1, Device #2 is constructed by transferring an exfoliated FeSe nanosheet with a symmetric geometric shape onto a pre-prepared electrode (Fig. 3(a)). The thickness of the FeSe nanosheet determined by AFM is about 20 nm (Fig. S4(b) in the ESM). As shown in Fig. 3(b), the temperature-dependent resistance measurement on Device #2 also displays a broad superconducting transition with T_c^{onset} = 6.2 K and T_c^{zero} = 4.9 K. As illustrated in Fig. 3(c), the *V*–*I* characteristics of Device #2 is measured at 2 K under the zero magnetic field, and the critical currents I_{c+} and $|I_{c-}|$ exhibit obvious non-reciprocal behaviors. This observation reveals that the field-free SDE persists in the device with a symmetric geometric shape, which is different from the previously reported field-free SDE in FeSe caused by the geometric asymmetry combined with the thermoelectric effect [41].

The temperature and magnetic field dependences of SDE in

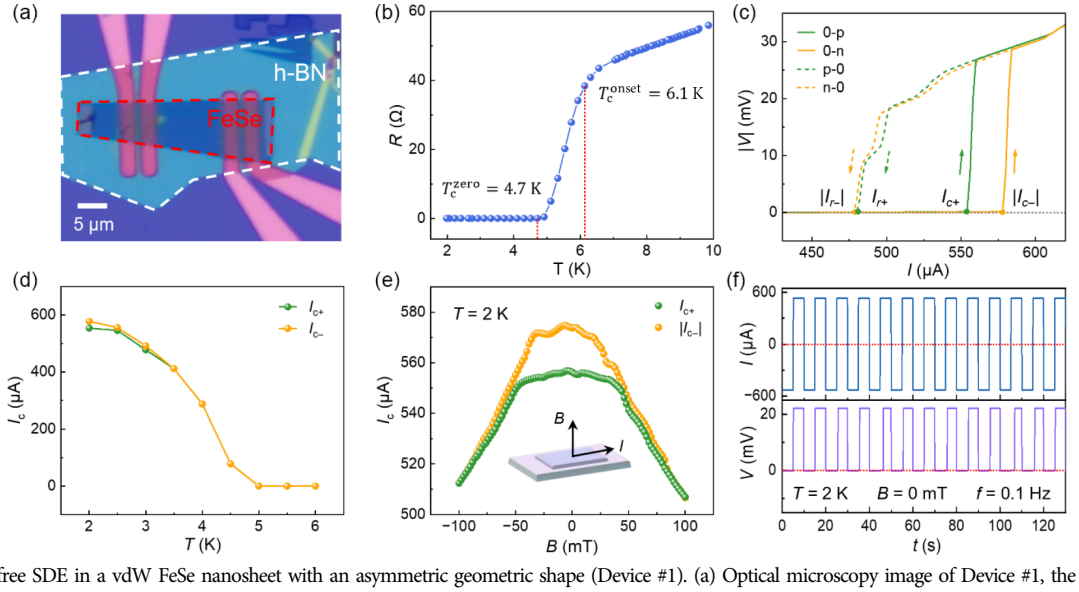

Figure 2 Field-free SDE in a vdW FeSe nanosheet with an asymmetric geometric shape (Device #1). (a) Optical microscopy image of Device #1, the dashed red and white lines outline the FeSe and top h-BN layers, respectively. (b) Temperature-dependent resistance $R(T)$ under the zero magnetic field, showing a superconducting transition with T_c^{onset} = 7.7 K and T_c^{zero} = 4.7 K. (c) Absolute *V*–*I* characteristics at 2 K under the zero magnetic field. Yellow/green shading denotes negative/positive bias regimes; solid and dashed curves represent superconducting-to-normal (S → N) and normal-to-superconducting (N → S) transitions, respectively. The positions of critical currents I_{c+}, $|I_{c-}|$, I_{r+} and $|I_{r-}|$ are marked. (d) Temperature dependence of critical currents (I_c) under the zero magnetic field. (e) Magnetic field dependence of I_{c+} and $|I_{c-}|$ at 2 K. The applied magnetic field B is perpendicular to the *ab*-plane of Device #1, as shown in the inset. (f) Rectification response of Device #1 at 2 K under the zero magnetic field. The top panel shows the applied square-wave excitation with an amplitude of 0.562 mA and frequency of 0.1 Hz. The bottom panel displays the corresponding measured voltage, which is zero during the negative current bias and finite during the positive current bias. The red dashed lines represent the zero level.

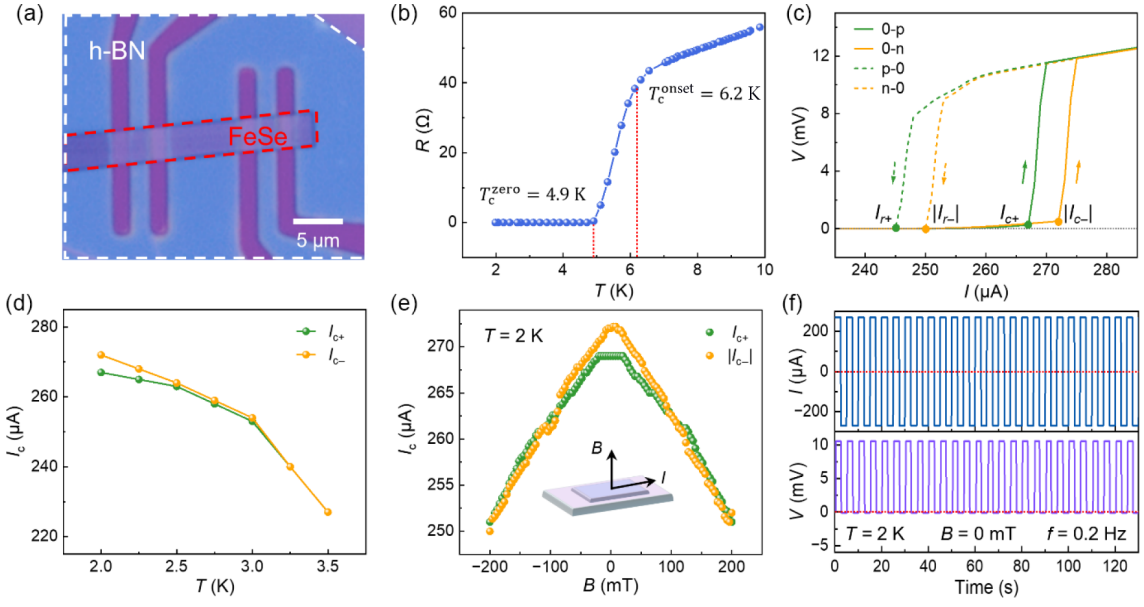

Figure 3 Field-free SDE in a vdW FeSe nanosheet with a symmetric geometric shape (Device #2). (a) Optical microscopy image of Device #2, with dashed red and white lines highlighting the FeSe and top h-BN layers, respectively. (b) Temperature-dependent resistance $R(T)$ under the zero magnetic field showing a superconducting transition with $T_c^{onset} = 6.2$ K and $T_c^{zero} = 4.9$ K. (c) Absolute V–I characteristics at 2 K under zero magnetic field. Negative (yellow) and positive (green) bias regions are shown, with solid and dashed lines indicating S → N and N → S transitions. The positions of critical currents I_{c+}, $|I_{c-}|$, I_{r+} and $|I_{r-}|$ are marked. (d) Temperature-dependent critical currents (I_c) under the zero magnetic field. (e) Field-dependent positive/negative critical current at 2 K. The applied magnetic field B is perpendicular to the *ab*-plane of the sample, as shown in the inset. (f) Rectification response of Device #2 at 2 K under the zero magnetic field. The top panel shows the applied square-wave excitation with an amplitude of 0.27 mA and frequency of 0.2 Hz. The bottom panel displays the corresponding measured voltage. The red dashed lines represent the zero level.

Device #2 are also investigated. As presented in Fig. 3(d), the temperature-dependent critical currents extracted from the V–I curves show monotonically decrease as the temperature increases. The difference between I_{c+} and $|I_{c-}|$ drops rapidly and completely vanishes above 3.5 K. The magnetic field dependence of I_{c+} and $|I_{c-}|$ demonstrate a pronounced nonreciprocity when the field is below 50 mT, and the sign of ΔI_c remains unchanged even reversing the direction of the magnetic field (Fig. 3(e)). These temperature- and field-dependent responses of SDE in Device #2 exhibit identical characteristics to those observed in Device #1. Furthermore, the half-wave rectification of superconducting diodes in Device #2 is tested by applying a low-frequency (0.2 Hz) square-wave current of 0.270 mA. As shown in Fig. 3(f) and Fig. S6(d) in the ESM, the negative half-cycles remain in the superconducting state, whereas the positive half-cycles drive the device into the normal state, generating large voltages. The rectification persists stable for over 400 consecutive cycles, proving the durability of the field-free SDE in FeSe nanosheets.

2.4 The intrinsic field-free SDE of the FeSe nanosheets

To verify the reproducibility of the field-free SDE, additional FeSe nanodevices (Device #3-Device #8) are fabricated and systematically measured. As shown in Figs. S7–S10 in the ESM, the V–I characteristics of the FeSe nanodevices display clear nonreciprocal behaviors. We have carried out a statistical analysis on the relationship between the diode efficiency η and the thickness as well as the geometric shape of the devices and the result reveals that η has no obvious correlation with the thickness and the geometric shape (Fig. S11 in the ESM). Furthermore, we have flipped the device under the zero magnetic field to check out the influence of the remanent field. As shown in Fig. 4(a), rotating the sample by 180° (0° → 180°) does not alter the polarity of SDE, indicating the field-free SDE is not attributed to the remanent fields of the superconducting magnet in our measurement system.

The Joule heating effect is a possible origin of asymmetric critical currents in V–I characteristics [11, 29]. In this situation, the polarity of SDE would switch for positive sweep (defined as n-p-n) and negative sweep (defined as p-n-p). However, as shown in Fig. 4(b), the V–I curves for positive and negative sweep totally overlap with each other. In addition, the stable rectification behavior over long-time cycles in Fig. S6(d) in the ESM further excludes the Joule-heating origin.

Random vortex trappings in FeSe nanosheets under the zero magnetic field could potentially cause the field-free SDE [28]. Therefore, we study the evolution of SDE with thermal cycles (2 K → 10 K → 2 K) under the zero magnetic field. As shown in Fig. 4(c), the distributions of critical currents with and without thermal cycles show no significant difference, indicating the field-free SDE observed in FeSe nanosheets is not attributed to random vortex trappings.

Asymmetric electrodes or interfacial contacts can also generate the non-reciprocal V–I transport [29]. As shown in Fig. S12 in the ESM, the contact resistances of Device #1, measured using the two-probe method, are 170.0, 139.5, and 161.5 Ω, respectively, indicating that contact-induced asymmetry is negligible. Moreover, the I–V curve of Device #1 at 10 K, shown in Fig. S13 in the ESM, is highly linear and passes through the origin, confirming good ohmic contacts and negligible contact capacitance. Importantly, the extrinsic asymmetry caused by asymmetric electrodes or interfacial contacts would manifest at all temperatures and magnetic fields. However, our measurements reveal the absence of non-reciprocal characteristics at the temperature above 3.5 K or under the magnetic fields exceeding 50 mT, which can exclude the effect of asymmetric electrodes or interfacial contacts. In summary,

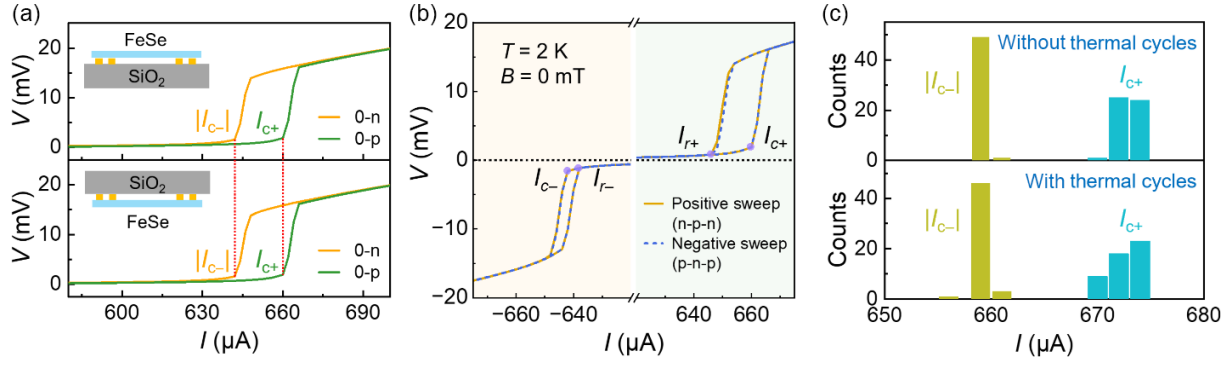

Figure 4 Intrinsic field-free SDE in vdW FeSe nanosheets. (a) Absolute V–I characteristics of the device with different setups at 2 K under the zero magnetic field. (b) V–I hysteresis measured by the positive sweeping (n-p-n, orange solid line) and negative sweeping (p-n-p, blue dashed line). (c) Critical current distributions at 2 K under the zero magnetic field. Top: measurements without thermal cycles. Bottom: measurements after thermal cycles (2 K → 10 K → 2 K).

systematic exclusion of plausible extrinsic mechanisms—including asymmetric geometry, residual magnetic fields, Joule heating effects, random vortex trappings and electrodes or interfacial contacts—provides definitive evidence that the field-free SDE originates from the intrinsic properties of FeSe nanosheets.

2.5 Possible origin of the intrinsic field-free SDE

Before discussing the origin of the intrinsic field-free SDE in FeSe nanosheets, we address a related study which attributes the field-free SDE to the interplay of a large thermoelectric response and geometrical asymmetry in FeSe [41]. Our experimental findings, however, point to a fundamentally different origin. Three crucial differences can be identified: (i) sample thickness and superconductivity: The previous work reports that the SDE is observed in the FeSe flake with the thickness of 114 nm and claims that the superconductivity is suppressed when the thickness falls below 20–30 nm. In contrast, the FeSe nanosheets in our work feature the thickness smaller than 20 nm (Fig. S4 in the ESM) and retain the stable superconductivity in this thickness regime. (ii) Geometric dependence: The SDE in the previous work appears only in the devices with asymmetric geometry, while the pronounced field-free SDE in our work can be observed in the devices with symmetric and asymmetric configurations (Figs. 2 and 3, and Figs. S7–S11 in the ESM). (iii) Magnetic-field-response: The previous study reports SDE persisting up to 500 mT, while SDE in our devices is completely suppressed under the magnetic field over 50 mT (Figs. 2(e) and 3(e)). This order-of-magnitude difference in the critical field implies the distinct underlying mechanisms. Collectively, the disparities in the sample thickness, the geometric shape, and the critical field demonstrate that the field-free SDE in our work originates from the different physical mechanism than the proposed thermoelectric-geometric mechanism [41].

The generation of SDE requires the simultaneous breaking of TRS and inversion symmetry. Inversion-symmetry breaking can arise from intrinsic lattice effects [21, 24, 42] or from extrinsic geometric asymmetry [43, 44], whereas TRS breaking can be induced by applying external magnetic fields [10, 12, 19–23, 26, 27], utilizing the proximity effect of a ferromagnetic layer [13, 15, 24], or relying on intrinsic properties of superconductors [17, 25, 28, 29]. Iron-based superconductors FeSe possess rich phase diagrams in which several symmetry-breaking orders are intertwined, and TRS breaking possibly origins from the following mechanisms: (i) mixed superconducting order parameters [37]: The combination of the near-degeneracy of s-wave and d-wave pairings and the sign-changing nematic order parameter across the Fermi surface in FeSe leads to TRS breaking below $T^* < T_c$. (ii) Hidden orders beyond nematicity [38]: FeSe enters a nematic phase below 90 K and coexists with superconductivity below $T_c \approx 9$ K, and high-resolution laser-based angle-resolved photoemission measurements show an additional order beyond nematic order emerges in FeSe, which can break either inversion or time-reversal symmetries. (iii) Unconventional order parameter near twin-boundary interfaces [39]: Scanning tunneling spectroscopy measurements reveal that the twin-boundary in FeSe can induce a fully gapped state, which gives rise to a possible twist of the order parameter, thus breaking TRS. Despite significant progress, the microscopic origin of TRS breaking in FeSe remains an open question due to its complex nature. The intrinsic field-free SDE observed in our work provides additional evidence that TRS and inversion symmetry are simultaneously broken in FeSe nanosheets.

3 Conclusions

In conclusion, we have demonstrated a pronounced field-free SDE in a single vdW FeSe nanosheet with a simple device configuration. Systematic investigations including sample geometries, residual magnetic fields, Joule heating effects, random vortex trappings and electrodes or interfacial contacts indicate that the field-free SDE is not induced by these extrinsic factors but by the intrinsic breaking of TRS in the superconducting state of FeSe nanosheets. Furthermore, this SDE maintains the same polarity over a wide range of both positive and negative magnetic fields, which can tolerate ubiquitous stray fields in electrical circuits. In addition, the devices remain stable after 400-cycle half-wave rectification under zero magnetic field. These features establish FeSe nanosheets as a promising platform to realize field-free superconducting diodes with a simple junction-free architecture for ultra-low power two-dimensional (2D) superconducting circuits.

4 Experimental section

4.1 Single crystal growth

High-quality FeSe single crystals were synthesized using a CVT method. High-purity Fe (Alfa Aesar, 99.998%) and Se (Alfa Aesar, 99.999%) were homogenized through mechanical milling and subsequently combined with transport agent $AlCl_3$/KCl in a glove box, which was then sealed in a quartz ampoule under high-vacuum conditions. The ampoule was placed in a two-zone

horizontal furnace, with the hot zone stabilized at 400 °C and the cold zone maintained at 350 °C over a period of two weeks. Finally, FeSe single crystals were obtained through sequential ultrasonic cleaning in deionized water to remove residual transport agents.

4.2 Characterization techniques

The crystalline structure analysis of FeSe was performed by the XRD. The magnetic properties of the crystals were measured using a magnetic properties measurement system (MPMS-3). The thicknesses of the FeSe layers were determined using a Cypher S atomic force microscope (Oxford Instruments, Asylum Research, Santa Barbara, USA). Samples for STEM characterization were prepared via focused ion beam (FIB) milling and performed on an aberration-corrected JEOL GRANDARM2 microscope operated at 200 kV. The beam convergence semi-angle was set to 32 mrad, while the collection semi-angles were 68–280 mrad for high-angle annular dark-field (HAADF) images and 17 mrad for annular bright-field (ABF) images.

4.3 Device fabrication

Bottom electrodes were fabricated on SiO_2/Si substrates using the ultraviolet lithography, followed by a thermal evaporation of Cr/Au (3/17 nm). Mechanical exfoliation and dry transfer processes were conducted in a glove box with controlled oxygen and moisture levels (O_2, H_2O < 0.1 ppm). The FeSe layer was transferred onto the electrodes using a modified PDMS-assisted dry transfer technique. The PDMS stamps were immersed in isopropyl alcohol for one week to remove surface residues and then naturally dried before use. The transferred FeSe flakes were subsequently encapsulated with a hBN layer for device protection.

4.4 Electrical transport measurements

Electrical transport measurements were performed in a Quantum Design Physical Property Measurement System (PPMS) with a Keithley 6221 current source and a Keithley 2182A nanovoltmeter. Electrical transport properties including resistance versus temperature (R–T) curves, voltage-current characteristics (V–I), differential conductance (dV/dI), and half-wave rectification were measured in a four-probe configuration.

4.5 Data processing

The critical current was defined as the *d.c.* current bias at which the first peak occurs in the differential conductance (dV/dI) curves. The I_{c+} and I_{c-} denote the critical currents in the positive and negative current directions, respectively. The superconducting transition temperature (T_c^{zero}) is defined as the temperature where the resistance falls to zero, while T_c^{onset} is defined as the intersection point between the extrapolated normal-state resistance line and the tangent line to the steepest slope of superconducting transition.

Electronic Supplementary Material: Supplementary material (Figs. S1–S13) is available in the online version of this article at https://doi.org/10.26599/NR.2026.94908621.

Data availability

All data needed to support the conclusions in the paper are presented in the manuscript and the Electronic Supplementary Material. Additional data related to this paper may be requested from the corresponding author upon request.

Acknowledgements

The work is supported by grants from the National Key Research and Development Projects of China (No. 2022YFA1204100), the National Natural Science Foundation of China (Nos. 62488201 and 12404066), the Innovation Program of Quantum Science and Technology (No. 2021ZD0302700), and the CAS Project for Young Scientists in Basic Research (No. YSBR-053). This research benefited from resources and support from the Electron Microscopy Center at the University of Chinese Academy of Sciences.

Declaration of competing interest

All the contributing authors report no conflict of interests in this work.

Author contribution statement

H.-J. G., X. L. and H. T. Y. designed the project. Y. C. H. and G. J. H. prepared the samples, performed the electrical transport measurements, and worked with the data. X. L. D. and Z. Y. W. L. provided the FeSe crystals. Z. W. and J. A. S. performed the STEM measurements. H. G. and S. H. L. performed the AFM measurements. L. H. B., J. L., and Z. Z. performed the XRD measurements. All authors participated in the data analysis and manuscript writing.

Use of AI statement

None.

References

[1] Scaff, J. H.; Ohl, R. S. Development of silicon crystal rectifiers for microwave radar receivers. *Bell Syst. Tech. J.* **1947**, *26*, 1–30.
[2] Shockley, W. The theory of p-n junctions in semiconductors and p-n junction transistors. *Bell Syst. Tech. J.* **1949**, *28*, 435–489.
[3] Tokura, Y.; Nagaosa, N. Nonreciprocal responses from non-centrosymmetric quantum materials. *Nat. Commun.* **2018**, *9*, 3740.
[4] Hu, J. P.; Wu, C. J.; Dai, X. Proposed design of a Josephson diode. *Phys. Rev. Lett.* **2007**, *99*, 067004.
[5] Jiang, K.; Hu, J. P. Superconducting diode effects. *Nat. Phys.* **2022**, *18*, 1145–1146.
[6] Moll, P. J. W.; Geshkenbein, V. B. Evolution of superconducting diodes. *Nat. Phys.* **2023**, *19*, 1379–1380.
[7] Ideue, T.; Iwasa, Y. Symmetry breaking and nonlinear electric transport in van der Waals nanostructures. *Annu. Rev. Condens. Matter Phys.* **2021**, *12*, 201–223.
[8] Nadeem, M.; Fuhrer, M. S.; Wang, X. L. The superconducting diode effect. *Nat. Rev. Phys.* **2023**, *5*, 558–577.
[9] Xiong, J. L.; Xie, J.; Cheng, B.; Dai, Y. D.; Cui, X. Y.; Wang, L. Z.; Liu, Z. L.; Zhou, J.; Wang, N. Z.; Xu, X. H. et al. Electrical switching of ising-superconducting nonreciprocity for quantum neuronal transistor. *Nat. Commun.* **2024**, *15*, 4953.
[10] Baumgartner, C.; Fuchs, L.; Costa, A.; Reinhardt, S.; Gronin, S.; Gardner, G. C.; Lindemann, T.; Manfra, M. J.; Faria Junior, P. E.; Kochan, D. et al. Supercurrent rectification and magnetochiral effects in symmetric Josephson junctions. *Nat. Nanotechnol.* **2022**, *17*, 39–44.
[11] Wu, H.; Wang, Y. J.; Xu, Y. F.; Sivakumar, P. K.; Pasco, C.; Filippozzi, U.; Parkin, S. S. P.; Zeng, Y. J.; McQueen, T.; Ali, M. N. The field-free Josephson diode in a van der Waals heterostructure. *Nature* **2022**, *604*, 653–656.
[12] Pal, B.; Chakraborty, A.; Sivakumar, P. K.; Davydova, M.; Gopi, A.

K.; Pandeya, A. K.; Krieger, J. A.; Zhang, Y.; Date, M.; Ju, S. L. et al. Josephson diode effect from Cooper pair momentum in a topological semimetal. *Nat. Phys.* **2022**, *18*, 1228–1233.
[13] Jeon, K. R.; Kim, J. K.; Yoon, J.; Jeon, J. C.; Han, H.; Cottet, A.; Kontos, T.; Parkin, S. S. P. Zero-field polarity-reversible Josephson supercurrent diodes enabled by a proximity-magnetized Pt barrier. *Nat. Mater.* **2022**, *21*, 1008–1013.
[14] Golod, T.; Krasnov, V. M. Demonstration of a superconducting diode-with-memory, operational at zero magnetic field with switchable nonreciprocity. *Nat. Commun.* **2022**, *13*, 3658.
[15] Trahms, M.; Melischek, L.; Steiner, J. F.; Mahendru, B.; Tamir, I.; Bogdanoff, N.; Peters, O.; Reecht, G.; Winkelmann, C. B.; von Oppen, F. et al. Diode effect in Josephson junctions with a single magnetic atom. *Nature* **2023**, *615*, 628–633.
[16] Díez-Mérida, J.; Díez-Carlón, A.; Yang, S. Y.; Xie, Y. M.; Gao, X. J.; Senior, J.; Watanabe, K.; Taniguchi, T.; Lu, X.; Higginbotham, A. P. et al. Symmetry-broken Josephson junctions and superconducting diodes in magic-angle twisted bilayer graphene. *Nat. Commun.* **2023**, *14*, 2396.
[17] Zhao, S. Y. F.; Cui, X. M.; Volkov, P. A.; Yoo, H.; Lee, S.; Gardener, J. A.; Akey, A. J.; Engelke, R.; Ronen, Y.; Zhong, R. D. et al. Time-reversal symmetry breaking superconductivity between twisted cuprate superconductors. *Science* **2023**, *382*, 1422–1427.
[18] Qiu, G.; Yang, H. Y.; Hu, L. H.; Zhang, H. R.; Chen, C. Y.; Lyu, Y.; Eckberg, C.; Deng, P.; Krylyuk, S.; Davydov, A. V. et al. Emergent ferromagnetism with superconductivity in Fe(Te,Se) van der Waals Josephson junctions. *Nat. Commun.* **2023**, *14*, 6691.
[19] Ghosh, S.; Patil, V.; Basu, A.; Kuldeep; Dutta, A.; Jangade, D. A.; Kulkarni, R.; Thamizhavel, A.; Steiner, J. F.; von Oppen, F. et al. High-temperature Josephson diode. *Nat. Mater.* **2024**, *23*, 612–618.
[20] Chen, P. B.; Wang, G. Q.; Ye, B. C.; Wang, J. H.; Zhou, L.; Tang, Z. Z.; Wang, L.; Wang, J. N.; Zhang, W. Q.; Mei, J. W. et al. Edelstein effect induced superconducting diode effect in inversion symmetry breaking $MoTe_2$ Josephson junctions. *Adv. Funct. Mater.* **2024**, *34*, 2311229.
[21] Ando, F.; Miyasaka, Y.; Li, T.; Ishizuka, J.; Arakawa, T.; Shiota, Y.; Moriyama, T.; Yanase, Y.; Ono, T. Observation of superconducting diode effect. *Nature* **2020**, *584*, 373–376.
[22] Yasuda, K.; Yasuda, H.; Liang, T.; Yoshimi, R.; Tsukazaki, A.; Takahashi, K. S.; Nagaosa, N.; Kawasaki, M.; Tokura, Y. Nonreciprocal charge transport at topological insulator/superconductor interface. *Nat. Commun.* **2019**, *10*, 2734.
[23] Itahashi, Y. M.; Ideue, T.; Saito, Y.; Shimizu, S.; Ouchi, T.; Nojima, T.; Iwasa, Y. Nonreciprocal transport in gate-induced polar superconductor $SrTiO_3$. *Sci. Adv.* **2020**, *6*, eaay9120.
[24] Narita, H.; Ishizuka, J.; Kawarazaki, R.; Kan, D.; Shiota, Y.; Moriyama, T.; Shimakawa, Y.; Ognev, A. V.; Samardak, A. S.; Yanase, Y. et al. Field-free superconducting diode effect in noncentrosymmetric superconductor/ferromagnet multilayers. *Nat. Nanotechnol.* **2022**, *17*, 823–828.
[25] Lin, J. X. Z.; Siriviboon, P.; Scammell, H. D.; Liu, S.; Rhodes, D.; Watanabe, K.; Taniguchi, T.; Hone, J.; Scheurer, M. S.; Li, J. I. A. Zero-field superconducting diode effect in small-twist-angle trilayer graphene. *Nat. Phys.* **2022**, *18*, 1221–1227.
[26] Bauriedl, L.; Bäuml, C.; Fuchs, L.; Baumgartner, C.; Paulik, N.; Bauer, J. M.; Lin, K. Q.; Lupton, J. M.; Taniguchi, T.; Watanabe, K. et al. Supercurrent diode effect and magnetochiral anisotropy in few-layer $NbSe_2$. *Nat. Commun.* **2022**, *13*, 4266.
[27] Gutfreund, A.; Matsuki, H.; Plastovets, V.; Noah, A.; Gorzawski, L.; Fridman, N.; Yang, G.; Buzdin, A.; Millo, O.; Robinson, J. W. A. et al. Direct observation of a superconducting vortex diode. *Nat. Commun.* **2023**, *14*, 1630.
[28] Le, T.; Pan, Z. M.; Xu, Z. K.; Liu, J. J.; Wang, J. L.; Lou, Z. F.; Yang, X. H.; Wang, Z. W.; Yao, Y. G.; Wu, C. J. et al. Superconducting diode effect and interference patterns in kagome CsV_3Sb_5. *Nature* **2024**, *630*, 64–69.
[29] Qi, S. C.; Ge, J.; Ji, C. C.; Ai, Y. W.; Ma, G. X.; Wang, Z. Q.; Cui, Z. H.; Liu, Y.; Wang, Z. Q.; Wang, J. High-temperature field-free superconducting diode effect in high-T_c cuprates. *Nat. Commun.* **2025**, *16*, 531.
[30] Strambini, E.; Spies, M.; Ligato, N.; Ilić, S.; Rouco, M.; González-Orellana, C.; Ilyn, M.; Rogero, C.; Bergeret, F. S.; Moodera, J. S. et al. Superconducting spintronic tunnel diode. *Nat. Commun.* **2022**, *13*, 2431.
[31] Castellani, M.; Medeiros, O.; Buzzi, A.; Foster, R. A.; Colangelo, M.; Berggren, K. K. A superconducting full-wave bridge rectifier. *Nat. Electron.* **2025**, *8*, 417–425.
[32] Ingla-Aynés, J.; Hou, Y. S.; Wang, S.; Chu, E. D.; Mukhanov, O. A.; Wei, P.; Moodera, J. S. Efficient superconducting diodes and rectifiers for quantum circuitry. *Nat. Electron.* **2025**, *8*, 411–416.
[33] Ortiz, B. R.; Teicher, S. M. L.; Hu, Y.; Zuo, J. L.; Sarte, P. M.; Schueller, E. C.; Abeykoon, A. M. M.; Krogstad, M. J.; Rosenkranz, S.; Osborn, R. et al. CsV_3Sb_5: A Z_2 Topological kagome metal with a superconducting ground state. *Phys. Rev. Lett.* **2020**, *125*, 247002.
[34] Zhao, H.; Li, H.; Ortiz, B. R.; Teicher, S. M. L.; Park, T.; Ye, M. X.; Wang, Z. Q.; Balents, L.; Wilson, S. D.; Zeljkovic, I. Cascade of correlated electron states in the kagome superconductor CsV_3Sb_5. *Nature* **2021**, *599*, 216–221.
[35] Yu, Y. J.; Ma, L. G.; Cai, P.; Zhong, R. D.; Ye, C.; Shen, J.; Gu, G. D.; Chen, X. H.; Zhang, Y. B. High-temperature superconductivity in monolayer $Bi_2Sr_2CaCu_2O_{8+\delta}$. *Nature* **2019**, *575*, 156–163.
[36] Sandilands, L. J.; Reijnders, A. A.; Su, A. H.; Baydina, V.; Xu, Z.; Yang, A.; Gu, G.; Pedersen, T.; Borondics, F.; Burch, K. S. Origin of the insulating state in exfoliated high-T_c two-dimensional atomic crystals. *Phys. Rev. B* **2014**, *90*, 081402(R).
[37] Kang, J.; Chubukov, A. V.; Fernandes, R. M. Time-reversal symmetry-breaking nematic superconductivity in FeSe. *Phys. Rev. B* **2018**, *98*, 064508.
[38] Li, C.; Wu, X. X.; Wang, L.; Liu, D. F.; Cai, Y. Q.; Wang, Y.; Gao, Q.; Song, C. Y.; Huang, J. W.; Dong, C. X. et al. Spectroscopic evidence for an additional symmetry breaking in the nematic state of FeSe superconductor. *Phys. Rev. X* **2020**, *10*, 031033.
[39] Watashige, T.; Tsutsumi, Y.; Hanaguri, T.; Kohsaka, Y.; Kasahara, S.; Furusaki, A.; Sigrist, M.; Meingast, C.; Wolf, T.; von Löhneysen, H. et al. Evidence for time-reversal symmetry breaking of the superconducting state near twin-boundary interfaces in FeSe revealed by scanning tunneling spectroscopy. *Phys. Rev. X* **2015**, *5*, 031022.
[40] Chen, G. Y.; Zhu, X. Y.; Yang, H.; Wen, H. H. Highly anisotropic superconducting gaps and possible evidence of antiferromagnetic order in FeSe single crystals. *Phys. Rev. B* **2017**, *96*, 064524.
[41] Nagata, U.; Aoki, M.; Daido, A.; Kasahara, S.; Kasahara, Y.; Ohshima, R.; Ando, Y.; Yanase, Y.; Matsuda, Y.; Shiraishi, M. Field-free superconducting diode effect in layered superconductor FeSe. *Phys. Rev. Lett.* **2025**, *134*, 236703.
[42] Wakatsuki, R.; Saito, Y.; Hoshino, S.; Itahashi, Y. M.; Ideue, T.; Ezawa, M.; Iwasa, Y.; Nagaosa, N. Nonreciprocal charge transport in noncentrosymmetric superconductors. *Sci. Adv.* **2017**, *3*, e1602390.
[43] Lyu, Y. Y.; Jiang, J.; Wang, Y. L.; Xiao, Z. L.; Dong, S. N.; Chen, Q. H.; Milošević, M. V.; Wang, H. B.; Divan, R.; Pearson, J. E. et al. Superconducting diode effect via conformal-mapped nanoholes. *Nat. Commun.* **2021**, *12*, 2703.
[44] He, Y.; Wang, Z. F.; Li, J. X.; Zhong, F. L.; Yang, H. Z.; Shi, K. W.; Wang, L.; Yang, G.; Zhao, W. S. Geometric asymmetry-enhanced nonreciprocal supercurrent transport revealed by second-harmonic response. *Adv. Funct. Mater.* **2025**, *35*, 2505766.